Tuning spin dynamics and localization near the metal-insulator transition in Fe/GaAs heterostructures

Yu-Sheng Ou, N. J. Harmon, Patrick Odenthal, R. K. Kawakami, M. E. Flatté, and E. Johnston-Halperin

Tuning Spin Dynamics and Localization Near the Metal-Insulator Transition in Fe/GaAs heterostructures

Yu-Sheng Ou[1], N. J. Harmon[2], Patrick Odenthal[3], R. K. Kawakami[1,3], M. E. Flatté[2], E. Johnston-Halperin[1†]

[1]*Department of Physics, The Ohio State University, Columbus, OH 43210-1117, USA*

[2]*Department of Physics & Astronomy, The University of Iowa, Iowa City, IA 52242-1479, USA*

[3]*Department of Physics & Astronomy, University of California, Riverside, CA 92521, USA*

Abstract

We present a simultaneous investigation of coherent spin dynamics in both localized and itinerant carriers in Fe/GaAs heterostructures using ultrafast and spin-resolved pump-probe spectroscopy. We find that for excitation densities that push the transient Fermi energy of photocarriers above the mobility edge there exist two distinct precession frequencies in the observed spin dynamics, allowing us to simultaneously monitor both localized and itinerant states. For low magnetic fields (below 3.00 T) the beat frequency between these two excitations evolves linearly, indicating that the nuclear polarization is saturated almost immediately and that the hyperfine coupling to these two states is comparable, despite the 20x enhancement in nuclear polarization provided by the presence of the Fe layer. At higher magnetic fields (above 3.00 T) the Zeeman energy drives reentrant localization of the photocarriers. Subtracting the constant hyperfine contribution from both sets of data allows us to extract the Lande g-factor for each state and estimate their energy relative to the bottom of the conduction band, yielding -2.16 meV and 17 meV for localized and itinerant states, respectively. This work advances our fundamental understanding

of spin-spin interactions between electron and nuclear spin species, as well as between localized and itinerant electronics states, and therefore has implications for future work in both spintronics and quantum information/computation.

I. Introduction

Defects play a central role in the developing fields of spintronics and quantum information, whether they are viewed as a loss channel for spin coherence in spin transport[1–8] or are themselves systems of interest for quantum computation[9,10] or quantum communication[11–14]. Many of these phenomena and proposed applications rely sensitively on the interplay between these defect states and itinerant carriers. For example, early work focused on maximizing the spin lifetime in semiconducting transport channels revealed that the lifetime is maximal in the vicinity of the metal-insulator transition[8,15–18] while many schemes for solid-state quantum computing rely on using conduction band spins to coherently bridge between defect states[9,10]. Analysis of these interactions is challenging due to the complexity of the multiple channels for spin coupling and interaction, ranging from the variety of ways defect scattering can interact with spin-orbit coupling (such as D'yakanov-Perel spin relaxation) to differences in hyperfine coupling due to potential differences in wave function overlap between localized and itinerant electrons[8,19,20]. However, despite the longstanding importance of these interactions, there have been relatively few studies to date that have been able to simultaneously explore the coherent spin dynamics of both localized and itinerant states within the same experiment[21,22].

Here we present a study of coherent spin dynamics in Fe/GaAs heterostructures where we tune the effective Fermi energy across the mobility edge by systematically tuning the density of photocarriers created by optical excitation. This is done using a time-resolved pump-probe technique that allows for the monitoring of the coherent spin dynamics in the sample, including both localized and itinerant electrons, and therefore reveals the differences, if any, between these two populations in the same sample and under the same experimental conditions. In addition, as we have previously demonstrated[2,23,24], the inclusion of the Fe layer significantly enhances the nuc-

lear spin polarization in these samples, i.e. the ferromagnetic proximity polarization (FPP) effect (see Sec. III for detailed discussion). This in turn dramatically amplifies the hyperfine interaction (roughly 20 times stronger than in isolated GaAs epilayers), allowing us to sensitively probe for any small differences in the hyperfine coupling between these two states. We find that for excitation densities that push the effective Fermi energy above the mobility edge there exist two distinct precession frequencies in the observed spin dynamics, allowing us to simultaneously monitor both localized and itinerant states at magnetic fields above 1.00 T. For magnetic fields below 3.00 T the beat frequency between these two excitations evolves linearly, indicating that the nuclear polarization is saturated almost immediately and that the hyperfine coupling to these two states is comparable. At higher magnetic fields (above 3.00 T) the Zeeman energy drives reentrant localization of the photocarriers. Subtracting the constant hyperfine contribution from both sets of data allows us to extract the Lande g-factor for each state and estimate their energy relative to the bottom of the conduction band, yielding -2.7 meV and 17.0 meV for localized and itinerant states, respectively.

II. Sample Synthesis and Ultrafast Spin Probes

The samples studied here are prepared via metal-organic chemical vapor deposition (MOCVD) and molecular beam epitaxy (MBE) in accordance with Refs. 2 and 24, with a layer structure of 10 nm MgO/10 nm Fe/0.2 nm MgO/120 nm Si-doped n-type GaAs (n = 7×10^{16}/cm^3)/400 nm In$_{0.5}$Ga$_{0.5}$P/n$^+$-type GaAs substrate. The Fe layer serves to enhance nuclear polarization via the FPP effect[2,25,26] and the thickness of the MgO layer between Fe and n-GaAs epitaxy layer is selected to optimize the FPP effect between Fe and n-GaAs while preventing interfacial intermixing which can give rise to an intermetallic FeGa phase[24]. The samples are

mounted face-down on 100 μm thick sapphire wafers so that the n^+-GaAs substrates can be removed by selective wet etching using the $In_{0.5}Ga_{0.5}P$ layer as a chemically-selective etch stop[27].

Time resolved Faraday rotation (TRFR) spectroscopy is employed to study the GaAs electron spin dynamics. A schematic of this technique is shown in Fig. 1(a); a circularly-polarized (CP) pump pulse, tuned to the band edge of GaAs (E_{pump}= 817 nm or 1.517 eV), excites a spin ensemble in GaAs along its propagation direction, which then starts to precess coherently in the presence of a transverse magnetic field, B_{tot}. The Faraday rotation angle (θ_{FR}) of a much weaker time-delayed linearly-polarized (LP) probe pulse (E_{probe}) directly measures the instantaneous component of this spin ensemble along its propagation direction. By systematically varying the delay time (Δt) between pump and probe pulse, the temporal evolution of the coherent photoexcited spin ensemble is revealed.

Laser pulses of 130-fs duration and 76 MHz repetition rate are generated by a mode-locked Ti: sapphire laser with central wavelength at 817 nm, and are split into pump and probe pulse trains whose power ratio is always kept above 10 with a time-averaged probe power of 0.55 mW (power density of 7.1 W/cm^2) for data discussed in Section IV and 0.31 mW (power density of 4 W/cm^2) for data discussed in Section V. All TRFR measurements are taken in a liquid Helium magneto-optical cryostat.

III. Enhancement of Nuclear Spin Polarization via FPP at Low Magnetic Field (B_{app} < 1.00 T)

The TRFR time scans taken at temperature T = 5 K and magnetic field B_{app}= 0.10 T for both the Fe/MgO/GaAs heterostructure and a GaAs control are shown in Fig. 1 (a). The time dependence of θ_{FR} can be described by the following equation:

$$\theta_{FR}(\Delta t) = A\left(e^{-\left(\Delta t/T_2^*\right)} + N_0 e^{-\left(\Delta t/T_h\right)}\right)\cos\left(2\pi f \Delta t + \theta\right), \quad (1)$$

where A is the maximal Faraday angle and N_0 is the ratio of photoexcited to equilibrium electrons ($N_0 = N_{ex}/n$) at $\Delta t = 0$, T_2^* is the inhomogeneous dephasing time of the photoexcited spin ensemble, T_h is the hole carrier recombination time, $f = \dfrac{g_{eff}\mu_B B_{tot}}{h}$ is the Larmor precession frequency caused by the total magnetic field $B_{tot} = B_{app} + B_n$, where B_{app} is the external applied field and B_n represents a hyperfine-driven effective field from GaAs nuclei[28], and θ is the phase of spin precession. The two exponential terms reflect the fact that the photoexcited holes, while not directly detected due to their rapid spin relaxation, do act to dephase the electron ensemble through the Bir-Aranov-Pikus mechanism until they recombine (typically in less than 100 ps). The clear difference in f (or equivalently, B_{tot}) between the Fe/MgO/GaAs and GaAs structures implies a variance in B_n between the two samples (roughly -0.20 T and +0.01 T, respectively). The magnitude and sign of B_n in Fe/MgO/GaAs has been attributed to a hyperpolarization of the Ga and As nuclei due to FPP effect[2,24–26], and is consistent with previous FPP measurements.

To confirm that the enhanced nuclear polarization is through the FPP effect in the Fe/MgO/GaAs heterostructure, we examined both B_{tot} and B_n as a function of applied field, B_{app}, at low field (0.80 T to -0.80 T). As can be seen in Fig. 1 (b) the dependence of B_{tot} on B_{app} has both a linear component (from the Zeeman dependence on B_{app}) and a component that tracks with the magnetization of the Fe layer, switching at fields below the experimental resolution (~0.002 T) and saturating at $B_{app} \sim 0.30$ T. This behavior is more clearly seen in the dependence of B_n on B_{app} in Fig. 1(c) where the linear Zeeman dependence has been subtracted, which confirms that the strong nuclear field observed in Fe/MgO/GaAs heterostructure indeed results from

the FPP effect. It should be noted that the bulk electron g-factor for GaAs[29] of -0.44 is used for the calculation of B_n.

IV. Identification of Localized and Itinerant Carriers at High Magnetic Field ($B_{app} \geq 1.00$ T)

Moving beyond the low field region, Fig. 2 (a) shows a TRFR time scan taken on a Fe/MgO/GaAs heterostructure at $T= 40$ K with an in-plane applied field $B_{app} = 5.00$ T and with a pump power density $I = 48$ W/cm^2. This time trace can be well described by equation (1). However, when the pump intensity increases to $I = 241$ W/cm^2, corresponding to a photocarrier density of 8.8×10^{16} cm^{-3}, we find that this single-frequency fitting function no longer provides a good description of the data (Fig. 2 (b)).

A fitting-function-independent approach to determine the possible origin of this discrepancy is to compare the fast Fourier transformation (FFT) power spectra for low- and high-intensity regimes (Fig. 2 (c)). The top panel of Fig. 2 (c) shows the FFT for the low power data shown in Fig. 2 (a), revealing a single peak whose width is consistent with the spin lifetime extracted from a fit of the time domain data to Eq. (1) ($T_2^* = 0.308$ ns). In contrast, the bottom panel of Fig. 2 (c) shows the FFT of the high power data shown in Fig. 2 (b), and in addition to the narrow peak seen in the top panel a broad peak at lower frequency is revealed. This suggests that the origin of the failure of Eq. (1) in the high power regime is due to the emergence of a second spin population with lower precession frequency and shorter lifetime.

To quantitatively explore this behavior, we add a second exponentially damped cosine function to eq. (1) and remove the exponential term that is related to the hole recombination time as it becomes commingled with the spin lifetime of the low-frequency component (see below),

$$\theta_{FR}(\Delta t) = A_H e^{\left(-\Delta t \Big/ (T_2^*)_H\right)} \cos\left(2\pi f_H \Delta t + \theta_H\right) + A_L e^{\left(-\Delta t \Big/ (T_2^*)_L\right)} \cos\left(2\pi f_L \Delta t + \theta_L\right), \quad (2)$$

where the first and second term represent the spin dynamics of the high and low frequency components, indicated by the subscripts H and L, respectively. The time scale of second spin population is found comparable to that of the hole recombination observed in the low power regime (< 100 ps), but its amplitude is orders of magnitude larger. As a result, for Δt< 100 ps, θ_{FR} is dominated by the second spin population, validating our decision to ignore the effect of recombination. The results of fitting the high power data with Eq. (2) can be seen in Fig. 2 (d), and the quality of the fit (χ^2) is reduced by an order of magnitude. The extracted values of $(T_2^*)_L$ and f_L (21 ps and 26.41 GHz, respectively) are consistent with the values extracted from the FFT in Fig. 2 (c), confirming the presence of a second precession frequency and consequently a second spin population in the sample that is only accessed by high pump fluence.

A potential explanation for this emergent state can be found from careful consideration of the schematic density of states (DOS) diagrams in Figs. 2 (e) − (f). Since the carrier concentration in the samples studied in this work is comparable to the room temperature metal insulator transition (MIT) in GaAs ($n_{MIT} \sim 3\times10^{16}$/cm^3)[8], we assume that the Si donor band (DB) hybridizes with the conduction band (CB), resulting in both occupied and unoccupied localized states at low energy and itinerant states at higher energy, as shown in Fig. 2 (e). This further suggests that the Fermi level, E_F, is located near the boundary between localized and delocalized states (direct measurement of the MIT in these samples is precluded by parasitic conduction in the InGaP layer). Note that while the center energy and energy width of the pump beam do not change, the fact that the ultrafast laser has a finite spectral width (~10 meV) means that as the intensity increases the high energy tail of the spectral distribution can continue to add carriers well above

the Fermi energy. As a result, the transient Fermi energy of the photocarriers will continue to increase with increasing pump fluence. If the initial doping of the GaAs is below the mobility edge of the metal insulator transition (as is the case here) then this can transiently drive the Fermi energy above that mobility edge, creating a population of itinerant photocarriers in parallel with the localized carriers excited at low pump power as is illustrated in Fig. 2 (f). A second consequence of the spectral width of the ultrafast laser is that the TRFR will be sensitive to the spin dynamics of all states (ΔE_{LP} or ΔE_{HP}) that fall within the spectral window of the probe laser pulse, i.e. it will simultaneously resolve the dynamics of both localized and itinerant carriers.

V. Coherent Spin Dynamics of Localized and Itinerant Carriers

As discussed in Section III, the presence of an Fe epilayer in these heterostructures serves to amplify the nuclear hyperfine coupling by roughly 20 times. This sensitivity, combined with the ability to simultaneously monitor the coherent spin dynamics of both localized and itinerant carriers, makes these samples an excellent testbed for exploring the impact of localization length on the hyperfine interaction in solids.

Complementing the Fermi energy tuning demonstrated in Section IV, here we vary the magnetic field from 1.00 T to 6.00 T at a variety of pump power densities ranging from 48 W/cm^2 to 455 W/cm^2 and at T= 40 K. Figure 3 shows the results of these studies focusing on the extracted Larmor precession frequencies for both the high- and low-frequency components (Figs. 3 (a) – (d)) and the corresponding FFTs (Figs. 3 (e) – (h)). As discussed previously, at I = 48 W/cm^2 there is only a single frequency component in both the time domain and frequency domain data (Figs. 3 (a) and 3 (e)), but at higher power densities a second low-frequency component emerges. In all cases the variation of frequency with applied magnetic field appears to be

dominated by linear contributions. In this regime the nuclear polarization is expected to be saturated, as the fields applied are larger than the saturation field of $Fe^{2,24}$, and so we tentatively assign this linear dispersion in the Zeeman interaction ($hf = g_{eff}\mu_B\left(B_{app} + B_n\right)$) to be due to the static applied field and the zero-field offset to be due to the saturated nuclear polarization for the first and second terms respectively. A careful inspection of Figs. 3 (b) – (d) suggests the presence of two distinct behaviors as a function of power.

Figure 4 explores this variation in more detail. Figure 4 (a) provides a detailed power dependence at fixed applied field (5.00 T), and shows a clear threshold behavior wherein at the very lowest power there is only a single frequency component, but as the power density is increased from 60 - 121 W/cm^2 a sharp variation in frequency is observed for the low frequency component. Above this threshold the low-frequency component stabilizes for the remaining range of powers accessible to the experiment (151 W/cm^2 – 455 W/cm^2). This sharp threshold behavior is hard to understand in the context of simply filling carriers into the parabolic conduction band, and strongly supports the idea of a density of states that includes a mobility threshold with diverging behavior for localized and delocalized states. Further support for this model can be found in estimating the density of photocarriers as a function of pump fluence, taking into account both the absorption coefficient of GaAs and the carrier lifetime of this sample. The result reveals that the threshold in pump power density corresponds to the regime where the density of photocarriers becomes comparable to the density of native carriers supplied by the Si donors in the GaAs matrix (7×10^{16}/cm^3), e.g. the regime where the density of photocarriers becomes sufficient to transiently perturb the Fermi energy to a significant degree.

This model can be further explored by considering the beat frequency between the high- and low-frequency components as a function of applied field. Figure 4 (b) shows such data for a

pump fluence of 108 W/cm^2 (red diamonds). Surprisingly, the beat frequency shows a maximum at a field of roughly 3.00 T, eventually returning to zero by 6.00 T. This non-monotonic behavior can be understood as the interaction between the g-factors of the localized and itinerant states (Fig. 4 (c)). Since the localized states have a higher g-factor, as the applied field increases they will move completely below the relatively modest Fermi energy of the photocarriers, resulting in a reentrant localization of the entire ensemble in the high field regime. Note that this mechanism applies only to pump fluences where the transient Fermi energy is slightly above the mobility edge (i.e. within the energy defined by the Zeeman energy). In a similar vein, the higher fluence curves also show a crossover, but as these higher densities of photocarriers exceed the total number of localized states in the system only a fraction of the ensemble becomes localized. Presumably, were higher fluences accessible without damaging the sample, then the linear regime of beat frequency would extend for the full field range as the relative number of localized and itinerant carriers would remain constant.

It is important to note that none of this discussion requires explicit consideration of the hyperfine coupling and associated effective field, B_n. This is quite surprising given the expected dependence of the Overhauser effect on the spatial distribution of the electron wavefunction and the myriad ways in which the localization length is modulated in these experiments. In fact, the beat frequency between the high- and low-frequency components extrapolates to 0 Hz at 0.00 T to within +/- 0.2 GHz, indicating that the effective field due to the hyperfine interaction is comparable for localized and delocalized carriers across all observed regimes despite the 20-fold enhancement provided by the Fe layer. Further, the fact that neither frequency evolves with pump power for power density greater than 150.6 W/cm^2 (Fig. 4 (a)) supports the assertion that the nuclear polarization is saturated throughout our experimental regime (if this were not the case the

increase in photocarrier density would be expected to generate a commensurate increase or decrease in precession frequency[24,30] depending on the sign of effective nuclear field with respect to external applied field).

This lack of sensitivity of the hyperfine field to localization length or pump power below 3.00 T allows for the extraction of an effective Lande g-factor (g_{eff}) as a function of pump power density for this field range (Fig. 4 (c)). The evolution of the g-factor closely tracks the evolution of precession frequency, and we can use a $k{\cdot}p$ model[31] to determine the following energy dependence of g factor in the conduction band:

$$g_{eff}(E) = -0.44 + 6.3 \times E(eV), (3)$$

where -0.44 is the g factor at the conduction minimum and E is the excess energy from the conduction band minimum. This analysis gives $E = -2.16$ meV for the localized carriers and $E = 17$ meV for the itinerant carriers.

VI. Conclusions

We have developed a system that allows for the simultaneous investigation of coherent spin dynamics in both localized and itinerant carriers in Fe/GaAs heterostructures. We find that for excitation densities that push the effective Fermi energy above the mobility edge there exist two distinct precession frequencies in the observed spin dynamics, allowing us to simultaneously monitor both localized and itinerant states. For low magnetic fields (below 3.00 T) the beat frequency between these two excitations evolves linearly, indicating that the nuclear polarization is saturated almost immediately and that the hyperfine coupling to these two states is the same to within experimental resolution. At higher magnetic fields (above 3.00 T) the Zeeman energy drives reentrant localization of the photocarriers. Subtracting the constant hyperfine con-

tribution from both sets of data allows us to extract the Lande g-factor for each state and estimate their energy relative to the bottom of the conduction band, yielding -2.16 meV and 17 meV for localized and itinerant states, respectively. This work advances our fundamental understanding of spin-spin interactions between electron and nuclear spin species, as well as between localized and itinerant electronics states, and therefore has implications for future work in both spintronics and quantum information/computation.

Acknowledgements

[†] To whom correspondence should be addressed. Email: ejh@mps.ohio-state.edu

[1] Y. Pu, P.M. Odenthal, R. Adur, J. Beardsley, A.G. Swartz, D. V. Pelekhov, M.E. Flatté, R.K. Kawakami, J. Pelz, P.C. Hammel, and E. Johnston-Halperin, Phys. Rev. Lett. **115**, 246602 (2015).

[2] Y.S. Ou, Y.H. Chiu, N.J. Harmon, P. Odenthal, M. Sheffield, M. Chilcote, R.K. Kawakami, M.E. Flatté, and E. Johnston-Halperin, Phys. Rev. Lett. **116**, 107201 (2016).

[3] N.J. Harmon, T.A. Peterson, C.C. Geppert, S.J. Patel, C.J. Palmstrøm, P.A. Crowell, and M.E. Flatté, Phys. Rev. B **92**, 140201 (2015).

[4] W. Han, R.K. Kawakami, M. Gmitra, and J. Fabian, Nat. Nanotechnol. **9**, 794 (2014).

[5] K. Pi, W. Han, K.M. McCreary, A.G. Swartz, Y. Li, and R.K. Kawakami, Phys. Rev. Lett. **104**, 187201 (2010).

[6] X. Lou, C. Adelmann, S.A. Crooker, E.S. Garlid, J. Zhang, K.S.M. Reddy, S.D. Flexner, C.J. Palmstrøm, and P.A. Crowell, Nat. Phys. **3**, 197 (2007).

[7] I. Appelbaum, B. Huang, and D.J. Monsma, Nature **447**, 295 (2007).

[8] J.M. Kikkawa and D.D. Awschalom, Phys. Rev. Lett. **80**, 4313 (1998).

[9] J.J. Pla, K.Y. Tan, J.P. Dehollain, W.H. Lim, J.J.L. Morton, D.N. Jamieson, A.S. Dzurak, and A. Morello, Nature **489**, 541 (2012).

[10] B.E. Kane, Nature **393**, 133 (1998).

[11] J.R. Weber, W.F. Koehl, J.B. Varley, A. Janotti, B.B. Buckley, C.G. Van de Walle, and D.D. Awschalom, Proc. Natl. Acad. Sci. U. S. A. **107**, 8513 (2010).

[12] W.F. Koehl, B.B. Buckley, F.J. Heremans, G. Calusine, and D.D. Awschalom, Nature **479**, (2011).

[13] L. Childress, M. V. Gurudev Dutt, J.M. Taylor, A.S. Zibrov, F. Jelezko, J. Wrachtrup, P.R. Hemmer, and M.D. Lukin, Science **314**, 281 (2006).

[14] A. Gruber, A. Dräbenstedt, C. Tietz, L. Fleury, J. Wrachtrup, and C. von Borczyskowski, Science **276**, 2012 (1997).

[15] B. Beschoten, E. Johnston-Halperin, D.K. Young, M. Poggio, J.E. Grimaldi, S. Keller, S.P. DenBaars, U.K. Mishra, E.L. Hu, and D.D. Awschalom, Phys. Rev. B **63**, 121202 (2001).

[16] V. Zarifis and T.G. Castner, Phys. Rev. B **36**, 6198 (1987).

[17] M. Römer, H. Bernien, G. Müller, D. Schuh, J. Hübner, and M. Oestreich, Phys. Rev. B **81**, 075216 (2010).

[18] J.H. Buß, T. Schupp, D.J. As, O. Brandt, D. Hägele, and J. Rudolph, Phys. Rev. B **94**, 235202 (2016).

[19] W.O. Putikka and R. Joynt, Phys. Rev. B **70**, 113201 (2004).

[20] N.J. Harmon, W.O. Putikka, and R. Joynt, Phys. Rev. B **81**, 085320 (2010).

[21] J. Huang, Y.S. Chen, A. Ludwig, D. Reuter, A.D. Wieck, and G. Bacher, Appl. Phys. Lett. **100**, 132103 (2012).

[22] L. Schreiber, M. Heidkamp, T. Rohleder, B. Beschoten, and G. Güntherodt, Arxiv: 0706.1884 (2007).

[23] Y.S. Ou, Y.H. Chiu, N.J. Harmon, P. Odenthal, M. Sheffield, M. Chilcote, R.K. Kawakami, M.E. Flatté, and E. Johnston-Halperin, in *Proc. SPIE 9551, Spintron. VIII*, edited by H.-J. Drouhin, J.-E. Wegrowe, and M. Razeghi (International Society for Optics and Photonics, 2015), p. 95510E.

[24] Y. Li, Y. Chye, Y.F. Chiang, K. Pi, W.H. Wang, J.M. Stephens, S. Mack, D.D. Awschalom, and R.K. Kawakami, Phys. Rev. Lett. **100**, 237205 (2008).

[25] R.K. Kawakami, Y. Kato, M. Hanson, I. Malajovich, J.M. Stephens, E. Johnston-Halperin, G. Salis, A.C. Gossard, and D.D. Awschalom, Science **294**, (2001).

[26] R.J. Epstein, I. Malajovich, R.K. Kawakami, Y. Chye, M. Hanson, P.M. Petroff, A.C. Gossard, and D.D. Awschalom, Phys. Rev. B **65**, 121202 (2002).

[27] H. Uchiyama, H. Ohta, T. Shiota, C. Takubo, K. Tanaka, and K. Mochizuki, J. Vac. Sci. Technol. B **24**, 664 (2006).

[28] F. Meier and B.P. Zakharcheni a, *Optical Orientation* (North-Holland, Amsterdam; New York, 1984).

[29] C. Weisbuch, C. Hermann, and G. Fishman, in *Proc. Twelfth Int. Conf. Phys. Semicond.* (Vieweg+Teubner Verlag, Wiesbaden, 1974), pp. 761−765.

[30] J.M. Kikkawa and D.D. Awschalom, Science **287**, 473 (2000).

[31] M.A. Hopkins, R.J. Nicholas, P. Pfeffer, W. Zawadzki, D. Gauthier, J.C. Portal, and M.A. DiForte-Poisson, Semicond. Sci. Technol. **2**, 568 (1987).

FIG. 1. (a) Schematic of time-resolved Faraday rotation (TRFR) measurement geometry. (b) Measured Faraday rotation (θ_{FR}) vs Δt for a Fe/MgO/GaAs heterostructure (solid circles) and a control GaAs epilayer (open circles) at T= 5 K and B_{app}= 0.10 T. The data are offset for clarity. (c) Top panel: total field B_{tot} (Larmor frequency f) as a function of B_{app} between +0.80 T and - 0.80 T at T = 5K. Bottom panel: nuclear field B_n (B_n= B_{tot} − B_{app}) as a function of B_{app}.

FIG. 2. Measured Faraday rotation angle (θ_{FR}) vs Δt for a Fe/MgO/GaAs heterostructure at T= 40 K and B_{app}= 5.00 T and at I= (a) 48 W/cm^2 and (b) 241 W/cm^2 and the fitting curves by eq. (1). (c) FFT spectra at I= 48 W/cm^2 (black) and I= 241 W/cm^2 (blue). The arrows label the characteristic frequencies appearing in (a) and (b). (d) The same TRFR time trace as in Fig. 1 (b) and the fitting curve by eq. (2). The insets in (a), (b) and (d) show the zoom-in TRFR time traces from Δt= 0.5 ns to 1.2 ns for clarity. Schematic density of states diagrams of GaAs and illustrations of state filling under (e) low pump excitation and (f) high pump excitation (see main text for details).

FIG. 3. Larmor frequency (f) as a function of B_{app} for both high-frequency (f_H, solid square) and low-frequency (f_L, open square) components at (a) I= 48 W/cm^2, (b) I= 108 W/cm^2, (c) I= 241 W/cm^2 and (d) I= 455 W/cm^2 and at T= 40 K. FFT spectra as a function of B_{app} at (e) I= 48 W/cm^2, (f) I= 108 W/cm^2 and (g) I= 241 W/cm^2 and (h) I= 455 W/cm^2.

FIG. 4. (a) Larmor frequency (f) as a function of pump power density (I) for both high-frequency (f_H, solid square) and low-frequency (f_L, open square) components at B_{app}= 5.00T. (b) Beat frequency (f_{beat}) as a function of B_{app} for I= 455 W/cm^2, 241 W/cm^2 and 108 W/cm^2. (c) Power density dependence of f/B_{app} and effective g factors for f_H and f_L components
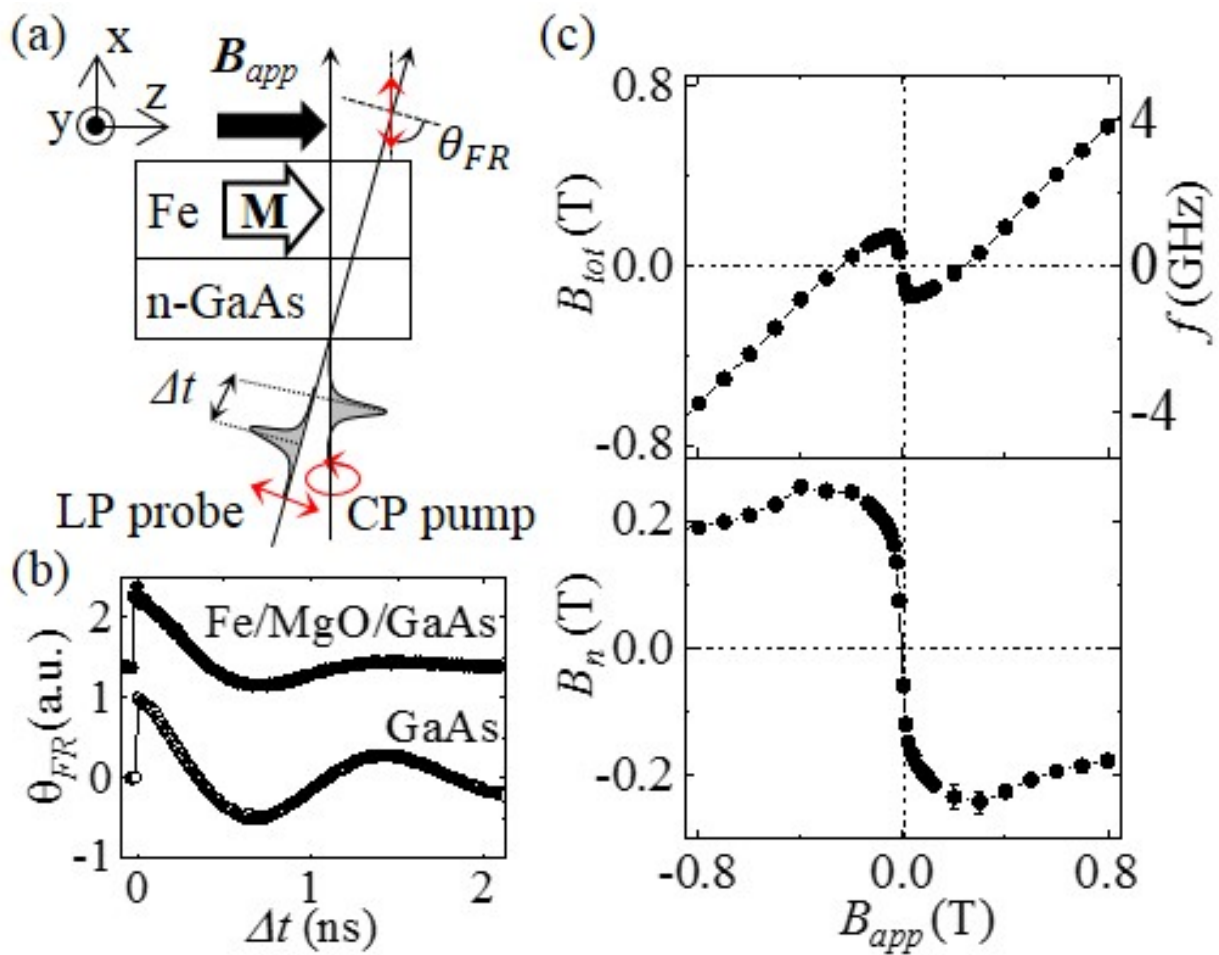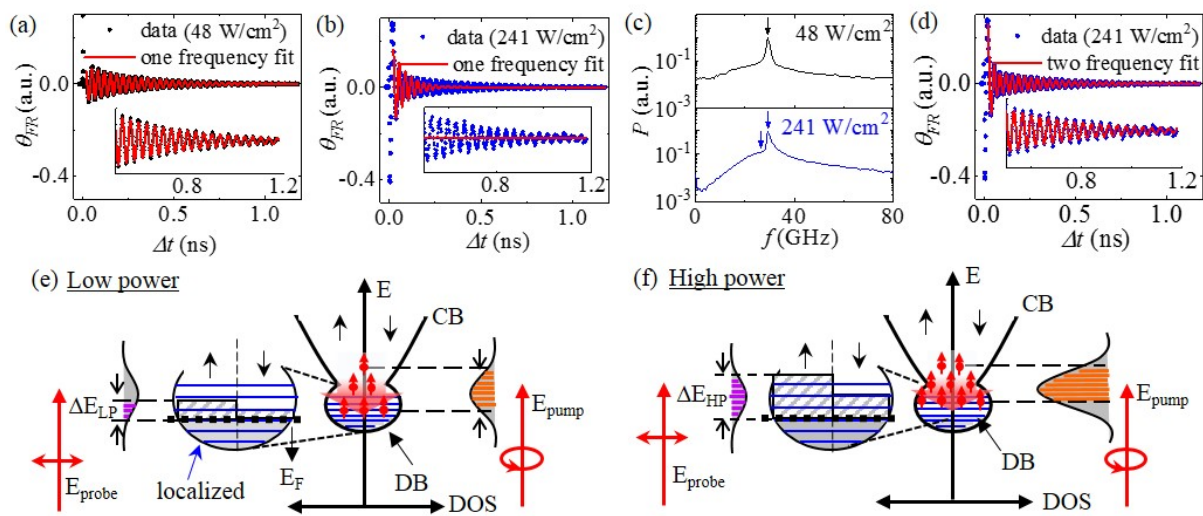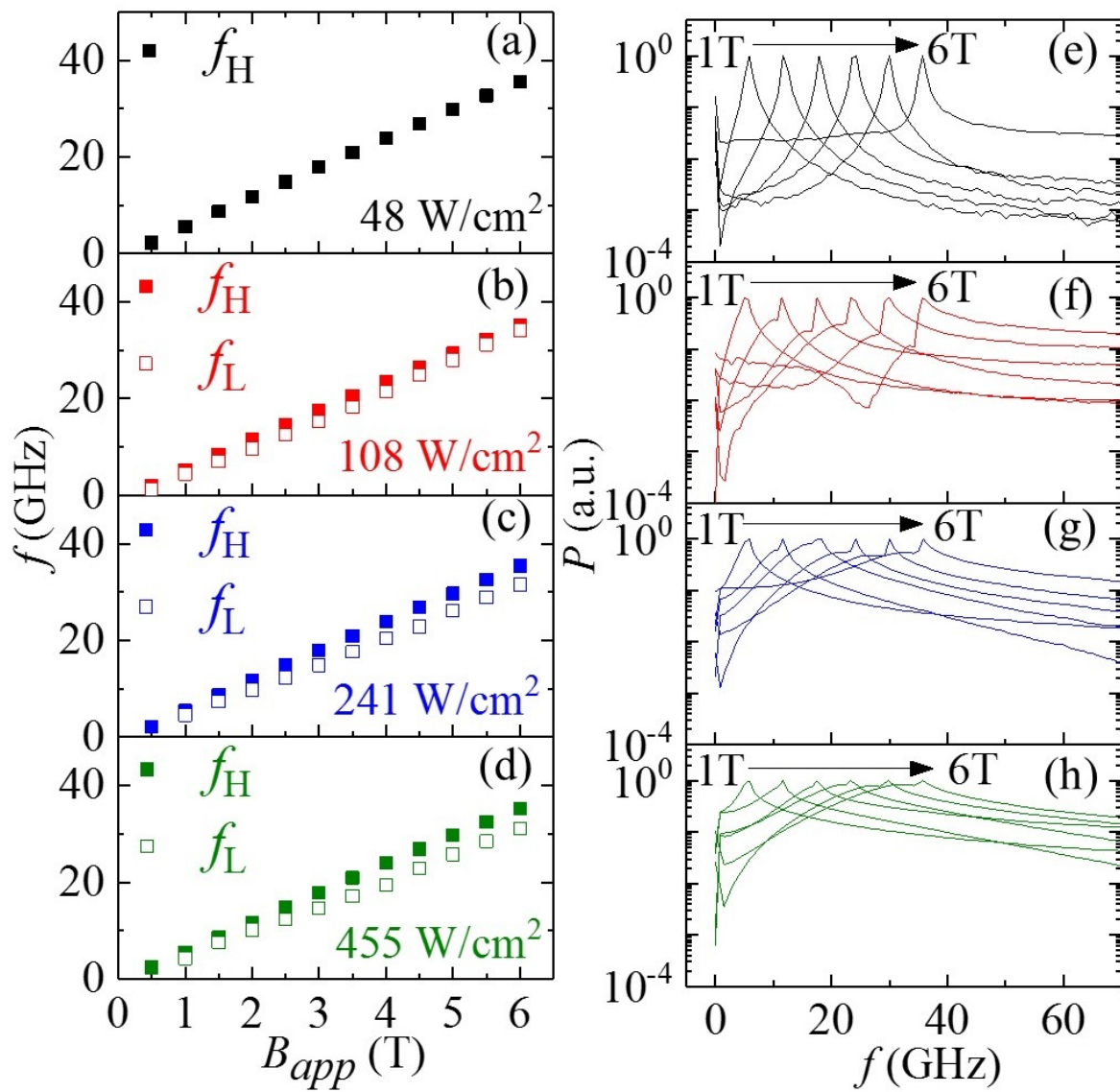
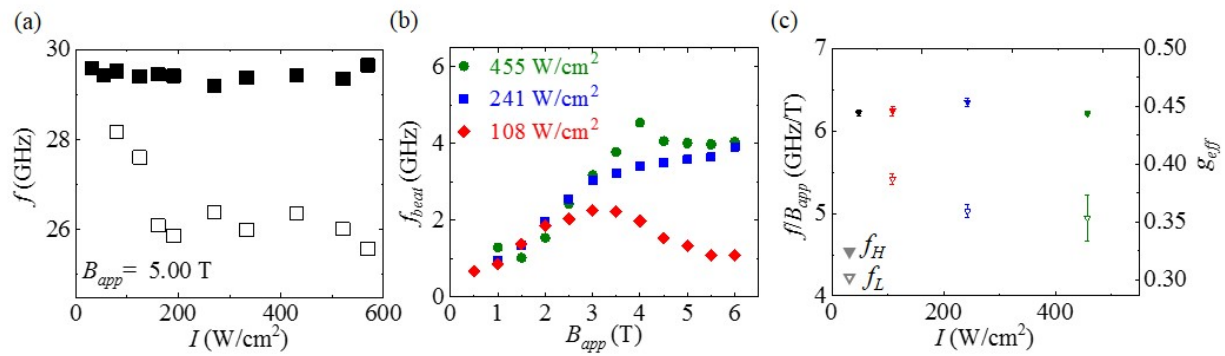**Figure 1** Yu-Sheng Ou

Figure 2 Yu-Sheng Ou

Figure 3 Yu-Sheng Ou

Figure 4 Yu-Sheng Ou